Journal of Biomedical Optics

SPIEDigitalLibrary.org/jbo

Microcirculation imaging based on full-range high-speed spectral domain correlation mapping optical coherence tomography

Hrebesh M. Subhash
Martin J. Leahy

SPIE

Microcirculation imaging based on full-range high-speed spectral domain correlation mapping optical coherence tomography

Hrebesh M. Subhash[a] and Martin J. Leahy[a,b]
[a]National University of Ireland, Tissue Optics and Microcirculation Imaging Facility, National Biophotonics and Imaging Platform, University Road, Galway, Ireland
[b]Royal College of Surgeons in Ireland, 123 St Stephens Green, Dublin 2, Ireland

Abstract. Microcirculation imaging is a key parameter for studying the pathophysiological processes of various disease conditions, in both clinical and fundamental research. A full-range spectral-domain correlation mapping optical coherence tomography (cm-OCT) method to obtain a complex-conjugate-free, full-range depth-resolved microcirculation map is presented. The proposed system is based on a high-speed spectrometer at 91 kHz with a modified scanning protocol to achieve higher acquisition speed to render cm-OCT images with high-speed and wide scan range. The mirror image elimination is based on linear phase modulation of B-frames by introducing a slight off-set of the probe beam with respect to the lateral scanning fast mirror's pivot axis. An algorithm that exploits the Hilbert transform to obtain a complex-conjugate-free image in conjunction with the cm-OCT algorithm is used to obtain full-range imaging of microcirculation within tissue beds *in vivo*. The estimated sensitivity of the system was around 105 dB near the zero-delay line with ~20 dB roll-off from ±0.5 to ±3 mm imaging-depth position. The estimated axial and lateral resolutions are ~12 and ~30 μm, respectively. A direct consequence of this complex conjugate artifact elimination is the enhanced flow imaging sensitivity for deep tissue imaging application by imaging through the most sensitive zero-delay line and doubling the imaging range. [DOI: 10.1117/1.JBO.19.2.021103]

Keywords: optical coherence tomography; spectral interferometry; microcirculation imaging; image processing; optical imaging; correlation mapping.

Paper 130208SSPRR received Apr. 3, 2013; revised manuscript received May 16, 2013; accepted for publication May 16, 2013; published online Jun. 27, 2013.

1 Introduction

Optical coherence tomography (OCT) is an emerging noninvasive imaging technique for anatomical and functional subsurface imaging with great potential for a wide range of biomedical applications.[1] Within the last decade, OCT and its functional variants has been successfully used for *in vivo* biomedical imaging for a range of applications, especially in the fields of ophthalmology and intravascular imaging, and has a potential for future "optical biopsy" in dermatology as well as for applications outside the field of biomedical imaging.[2] Through developments of endoscopic probes, it can be applied to epithelial cancers on any accessible surface. With the recent advances in light source and detection technology, the development in OCT has shifted toward spectral-domain OCT (SDOCT) and swept-source OCT (SSOCT), since it has been shown that these frequency-domain OCT versions have advantages in terms of acquisition speed and sensitivity, as compared to time-domain OCT.[3–5] Recently, the functional extension of the OCT technique to image depth-resolved microcirculation has become a very promising area of research. There is a growing interest in the field of development of various types of OCT-based angiographic techniques, which aims to visualize the lumens and architecture of blood vessels in many clinical and fundamental areas of research, including cardiology, dermatology, neurology, ophthalmology, small animal imaging studies, and so forth.[6] OCT-based angiography techniques utilize the red blood cell scattering dynamics as contrast mechanism, which exhibits phase or amplitude fluctuations over time, while the static tissue scattering is relatively constant over time. There are mainly three categories of OCT-based angiography methods, which are essentially based on the utilization of the complex nature of the OCT signal to obtain the microcirculation map: phase-based techniques,[7–11] magnitude-based techniques,[12–17] and techniques that use the complex data,[18–23] incorporating both magnitude and phase information.

Optical Doppler tomography or Doppler OCT (D-OCT) is an example of a purely phase-based technique for imaging flow velocity of moving particles in a highly scattering medium.[7,8] In D-OCT, based on SD or SS implementation, the blood circulation is evaluated by taking the phase difference between adjacent A-line scans in B-frame.[7–11] Although the D-OCT algorithm is capable of imaging and quantification of flow velocity in relatively large blood vessels,[8,24] the velocity of the dynamic component of small vessels are underestimated due to the presence of static scattering.[20,24] Moreover, this technique is sensitive to the Doppler angle and is unable to detect the flow components perpendicular to the scanning beam.[25,26] Phase variance[11] and Doppler variance are other alternative phase-based methods developed for the visualization of microcirculation.[27]

Address all correspondence to: Hrebesh M. Subhash, National University of Ireland, Tissue Optics and Microcirculation Imaging Facility, National Biophotonics and Imaging Platform, Galway, Ireland. Tel: +353-91-49-2824; Fax: +353-91-494584; E-mail: hrebeshms@gmail.com

Unlike D-OCT, these methods are insensitive to Doppler angle. These methods are capable of detecting both transverse and axial flow, and do not require any nonperpendicular beam of incidence. Optical microangiography (OMAG)[18] and rapid volumetric angiography[21] are examples of techniques that utilize the complex field of both amplitude and phase of the OCT signal. OMAG utilizes a modified Hilbert-transform-based algorithm to separate the dynamic scatterers from static tissue background. By applying the OMAG algorithm along the slow scanning axis, high-sensitivity imaging of capillary flow can be achieved. For obtaining high sensitivity, OMAG requires the removal of bulk motion artifact by resolving the Doppler shift. Recently, the flow sensitivity of OMAG has been enhanced using a new processing and scanning protocol termed ultra-high-sensitive OMAG,[20] which utilizes the OMAG algorithm in the C-scan direction to obtain high-sensitivity flow map. To date, based on SDOCT technology, a couple of OCT angiography techniques utilizing the complex field of the OCT signal have been proposed by various research groups.[28–30] However, phase-based methods are more susceptible to the axial movement of bulk tissue and other sources of motion artifacts such as galvanometer jitter, physiological motion, and thermal drift, which require more sophisticated methods of the bulk motion phase correction. On the other hand, magnitude-based angiography techniques are purely based on the amplitude of the OCT signal. Techniques termed speckle-variance OCT[12,13] and split-spectrum amplitude decorrelation angiography[16] are examples of magnitude-based methods. Unlike phase-based technique, magnitude-based techniques are insensitive to bulk phase changes and, therefore, do not require any sophisticated phase correction methods.

Correlation mapping OCT (cm-OCT)[14,15] is another purely magnitude-based angiography technique developed by our group, which takes advantage of the time-varying speckle effect, which is normally dominant in the vicinity of vascular regions compared to static tissue region. It utilizes the correlation coefficient as a direct measurement of decorrelation between two adjacent B-frames to enhance the visibility of microcirculation. By using an unmodified commercial SSOCT system (OCM1300SS, Thorlabs Inc., Newton, NJ) with an axial scan rate of 16 kHz, we have successfully used cm-OCT for a number of biological imaging applications, such as small animal cerebral perfusion imaging, human cutaneous and volar forearm microcirculation imaging, etc. However, the reported cm-OCT was based on a commercial SSOCT system with a relatively slow axial-scan rate and which does not provide direct control over the scan patterns to implement repeated scanning over the same B-scan location to provide better correlation contrast. Thus, this system requires a dense scan protocol to accomplish better correlation between adjacent B-frames such that the interframe separation was within the resolution limit of the OCT system to ensure strong correlation between adjacent frames. The overall acquisition time for a scan area of 3 mm × 3 mm × 3 mm (1024 × 1024 × 512) was ~70 s, which drastically limits the overall system performance for real-world *in vivo* imaging applications.

In this paper, in order to overcome these limitations, we present an improved cm-OCT technique based on a custom-built high-speed SDOCT system and introduced a modified scanning protocol with full-range complex-conjugate-free imaging capability. The modified scanning protocol measures repeated B-scans at the same location to generate a high-sensitivity correlation map between successive B-frames and a constant modulation frequency was introduced into the spatial interferograms to provide complex-conjugate-free cm-OCT images. Thus, this method has the additional advantages of doubling the depth range, which enables access to the high-sensitivity imaging region close to the zero optical path delay (OPD). We implemented the full-range imaging by offsetting the sample beam from the pivot axis of the x-scanner.[28–32] This causes a path length modulation during x-scanning, thus introducing a modulation frequency in the B-scan interferograms. Another advantage of this method is that any additional phase shifting elements normally needed to realize frequency modulation in a single B-scan are avoided. Furthermore, the modulation frequency is inherently given by the system itself. These aspects provide us a potential to achieve high-speed full-range complex cm-OCT imaging without restriction on any additional hardware component, and without limitation on the imaging speed, which is important for *in vivo* imaging applications. This scanning protocol can provide better background suppression and wide scanning with a relatively short acquisition time.

2 Experimental Setup and Methods

2.1 *High-Speed Full-Range Spectral-Domain OCT System*

The schematic of the high-speed full-range SDOCT setup is depicted in Fig. 1. A broadband 1310 nm superluminescent diode with bandwidth of 83 nm (SLD, Dense Light, Singapore) was coupled into the interferometer, via an optical coupler. The spectrometer consisted of a 50-mm focal length collimator, a 1145 − lines/mm transmitting grating, an achromatic lens with a 100-mm focal length, and a 14-bit, 1024-pixels InGaAs line scan camera (SU1024LDH2, Goodrich Ltd., USA) with a maximum acquisition rate of 91 kHz. This spectrometer setup had a spectral resolution of 0.1432 nm, which gave a maximum imaging range of ~6 mm (in air). The measured axial imaging resolution of the system was ~12 μm in air (~9.2 μm in human skin). The sample arm consists of a pair of galvanometric driven mirrors and a 5× objective (LSM003Thorlabs Inc.), which provided a lateral resolution of ~30 μm. The measured sensitivity of the system was ~105 dB near the zero-delay line. The sensitivity dropoff of the system was ~20 dB at a depth range of ±3 mm.

The inset in Fig. 1 shows the scanner mirror offset-based phase modulation technique implemented for obtaining the complex-conjugate-free full-range OCT. This is a direct adoption of the modulation technique originally developed by Podoleanu et al.,[28] for generating a stable carrier frequency for an en-face OCT scanning system, and further developed by several other groups.[29–31] To achieve full-range cm-OCT imaging, we first added a constant phase shift into adjacent A-lines by offsetting the incident beam of sample arm away from the pivot of the x-scanner. The resultant modulation frequency f_c can be expressed as[32]

$$f_c = 4\delta\omega/\lambda, \tag{1}$$

where δ is the offset displacement of the sample beam away from the pivot point on the x-scanner, as shown in the inset of Fig. 1(b), and ω is the angular scanning frequency of the x-scanner during imaging. In our case, the displacement δ was set 1.6 mm away from the pivot point. Thus, with a

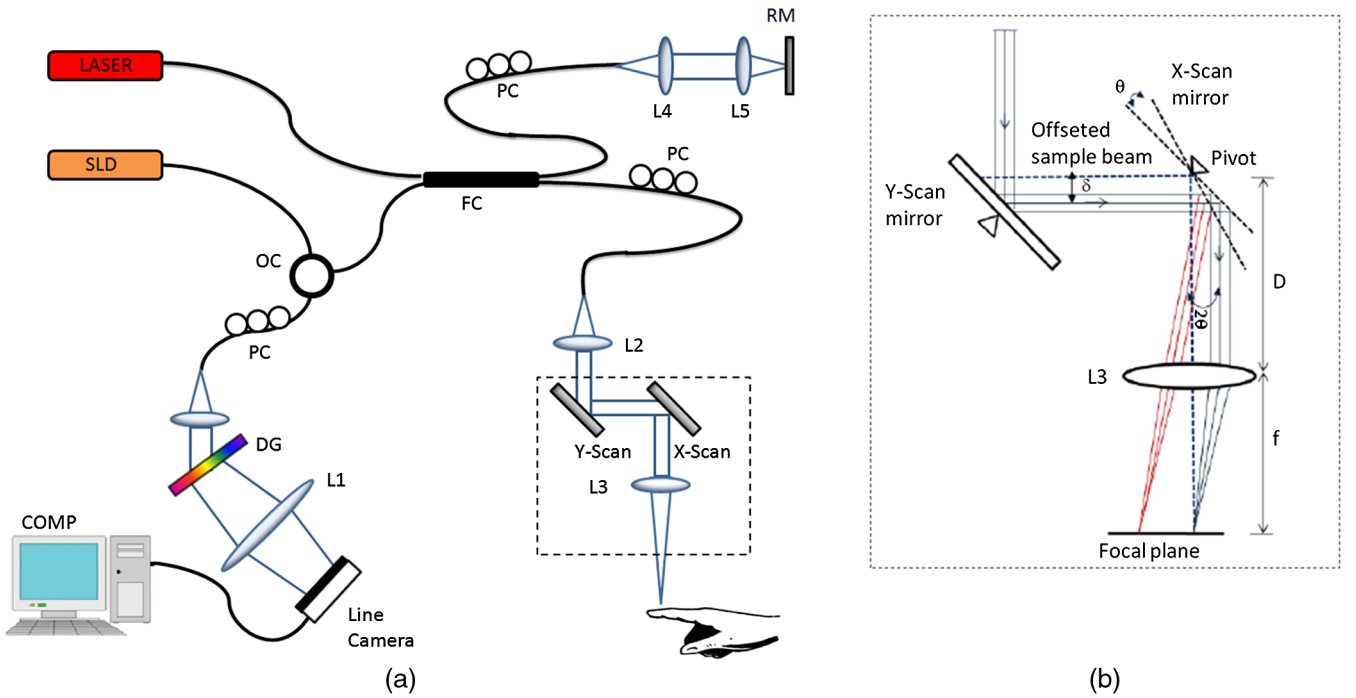

Fig. 1 (a) Experimental setup of the high-speed spectral-domain OCT system. DG, diffraction grating; L1 to L5, lenses; PC, polarization controller; OC, optical circulator; FC, fiber coupler; RM, reference mirror. (b) Schematic of the beam offset method at the sample arm. L, objective lens; θ, scanning angle; δ, beam offset displacement.

B-frame scanning frequency of 150 Hz, the set angular velocity was ~4.7 rad/s, which corresponds to a modulation of ~22.96 kHz.

2.2 *Scanning Protocol*

A modified scanning protocol was implemented with LabVIEW and National Instrument's (NI) analogue board (NI PCI-6713) to specifically enable fast acquisition and processing of correlation mapping. In this study, the camera integration time was set at 6.96 μs for imaging, allowing $\sim < 1$ μs for downloading the spectral data from line detector (1024 pixels, A scan) to the host computer via CameraLink™ and a high-speed frame grabber board (NI PCI 1428, NI, USA). This configuration determined a line scan rate of ~91 kHz for the camera. With this configuration, the B-scan frame rate of the system was set to ~150 frames per second. To achieve three-dimensional (3-D) imaging, we used two galvo-scanners to raster-scan the focused beam spot across the sample in the fast-scan direction (i.e., B-scan) and 512 A-lines were set to cover 4 mm. Unlike the previous version of the cm-OCT scanning protocol, which requires a 3-D volume with dense sampling of B-frames, this modified scanning protocol captures repeated B-frames in the same lateral position to provide high-contrast correlation. In the slow-scan direction (i.e., C-scan), 200 sampling positions were set to cover a 4 mm distance and four repeated B-scans were set at every C-scan position to reconstruct the cm-OCT flow map. Thus, the total acquisition time to record 800 B-frames was ~5.4 s. By implementing this repeated scanning protocol, the texture pattern artifact caused by the difference in optical heterogeneity of tissue could be suppressed.[33] Moreover, the repeated scan protocol provides the calculation of the correlation map in an intralocation manner within the sample, which allows additional capability of providing wide-field imaging.

2.3 *Full-Range Image Reconstruction and Correlation Mapping Algorithm*

Figure 2 shows the schematic of a flow diagram illustrating the implemented scanning protocol and image reconstruction method. As described above, the scan protocol samples the same lateral position four times per volume. For 3-D imaging, we set a scan volume of 4 mm × 3 mm × 6 mm (xyz) with a voxel size of 512 × 1024 × 200 (xyz). In order to obtain the full-range amplitude profile, an algorithm based on Hilbert transform was employed. Before applying this full-range reconstruction algorithm, the autocorrelation, self-cross correlation, and fixed camera noises inherent with the SDOCT were eliminated by subtracting a reference spectrum, which is obtained by taking the ensemble average of the whole volumetric fringe data. Then the subtracted spectra were remapped from λ-domain to k-domain by the spline interpolation method. To obtain the full-range amplitude OCT image, first, the Hilbert transformation is performed along the B-scan direction to obtain the complex interferograms. Then the Fourier transformation is applied along the k space value (in the z-direction).

For volumetric reconstruction of microcirculation, the correlation mapping algorithm is directly applied to the reconstructed full-range amplitude OCT images as shown in Fig. 2. Briefly, cm-OCT is an interframe microcirculation imaging method based on purely processing the amplitude of the OCT signal. First, two full-range amplitude OCT images were calculated by averaging the two consecutive frames of the four OCT images captured at the same lateral position to obtain good sensitivity. Then the correlation between these two full-range OCT B-frames is determined by cross-correlating a grid from frame A (average of frames 1 and 2) to the same grid position from frame B (average of frames 3 and 4) using the following equation:

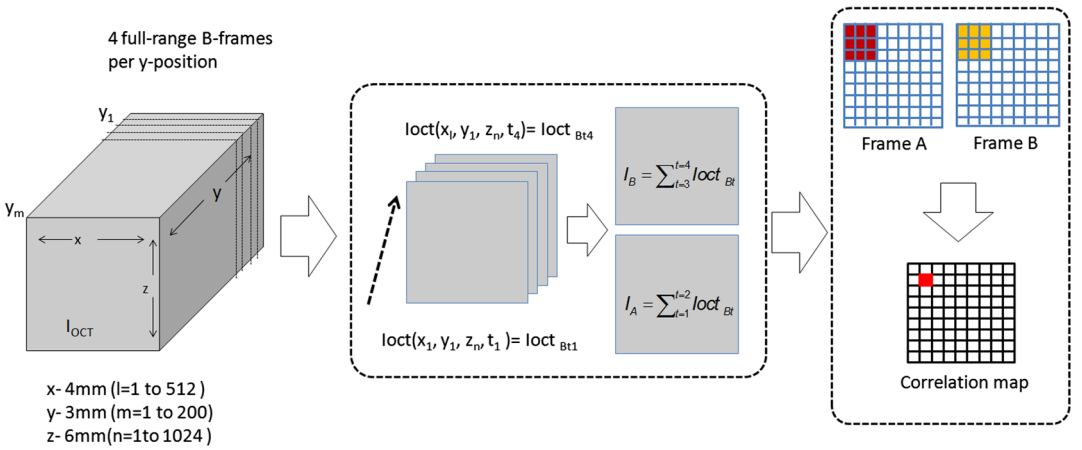

Fig. 2 Flow chart of correlation-mapping image processing based on the modified scanning protocol.

$$\mathrm{cmOCT}(x,y)=\sum_{p=0}^{M}\sum_{q=0}^{N}\frac{[I_A(x+p,y+q)-\bar{I}_A(x,y)][I_B(x+p,y+q)-\bar{I}_B(x,y)]}{\sqrt{[I_A(x+p,y+q)-\bar{I}_A(x,y)]^2[I_B(x+p,y+q)-\bar{I}_B(x,y)]^2}}, \tag{2}$$

where M and N are the grid size and $\bar{I}$ is the grid's mean value. This grid is then shifted across the entire XY full-range OCT image and a two-dimensional correlation map is generated. The resulting correlation map contains values in the range of -1 to $+1$, indicating negative strong correlation and strong correlation, respectively. In this particular study, we optimize the static tissue features with a threshold correlation value >0.6 and the correlation value ranging between $+0.6$ to -0.6 is used for mapping the microcirculation. A grid kernel size of 5×5 was empirically chosen to obtain optimal performance with the trade-off of processing time. Custom-written software based on Java was used to implement the correlation-mapping algorithm, which includes the background noise suppression using a structural mas k and enables the reconstruction of both structural and microcirculation map.[15] This software requires only ~30 s to process and render a volumetric image of size $512\times1024\times200$ $(x\times z\times y)$.

3 Results and Discussion

3.1 *Phantom Study*

To test the feasibility of our proposed complex-conjugate-free full-range cm-OCT method, we first performed a flow phantom experiment with intralipid particles in a set of three translucent capillary tubes. The flow phantom was made from synthetic clay (Blu-Tack®, Bostik, Wauwatosa, Wisconsin) to simulate the background optical heterogeneity of the tissue, and three capillary tubes with an inner diameter of ~500 μm were submerged in this. The capillary tube was filled with a 2% intralipid solution, which was allowed to move under Brownian motion. For imaging, the flow phantom was placed under the scan head of the imaging system such that the sample remained at one side of the zero-OPD; then 800 B-frame images were taken over an area of 4 mm$(x)\times6$ mm (z) in approximately 5.4 s. While imaging, we axially displaced the sample in order across the zero-OPD to demonstrate the system capability of enhanced sensitivity and full-range extended depth-imaging capability.

Figure 3(a) (Video 1) shows the cross-sectional structural fly-through images of the flow phantom using standard spectral-domain processing algorithm, by applying the correlation-mapping algorithm to the same OCT amplitude images; the corresponding cross-sectional flow images are shown in Fig. 3(b) (Video 2). With this standard spectral-domain processing, it is clearly evident that the true object structural and flow images are obscured by the overlapping mirror image due to the complex conjugate artifact. However, Fig. 3(c) (Video 3) and 3(d) (Video 4) shows the result of structural and cm-OCT flow maps derived from the same set of spectral fringe data with full-range complex conjugate removal algorithm. As can be seen in Fig. 3(c) and 3(d), the complex conjugate mirror artifact could be efficiently suppressed in both structural and correlation-mapping microcirculation image.

3.2 *In vivo Imaging of Microcirculation in Human Skin*

Next, in order to evaluate the system performance for *in vivo* imaging applications, we imaged the dorsal skin over the distal phalanx of left little finger of a healthy human volunteer. In order to perform imaging, the little finger of the volunteer was fixed on a home-built imaging platform, such that the dorsal skin of the little finger faces the OCT probing beam. Imaging was performed over an area of 4 mm $\times$ 3 mm at the location of the nail-fold area (i.e., dorsal skin) over the distal phalanx of the little finger as shown in Fig. 4(a). The scanning protocol was set to capture 512 A-scans per B-frame over a scan distance of 4 mm. For 3-D imaging, we acquired 200 B-scan sampling positions over a scan range of 3 mm, such that four repeated B-scans were captured at every C-scan position. The set B-frame rate was 150 Hz, and this scan rate was adequate to eliminate most of the effect of residual bulk tissue motion artifact. Thus, the 3-D volumetric data consisted of a total of 800 B-frames with 512 A-lines per B-frame. The volumetric data obtained was processed using the outlined cm-OCT method

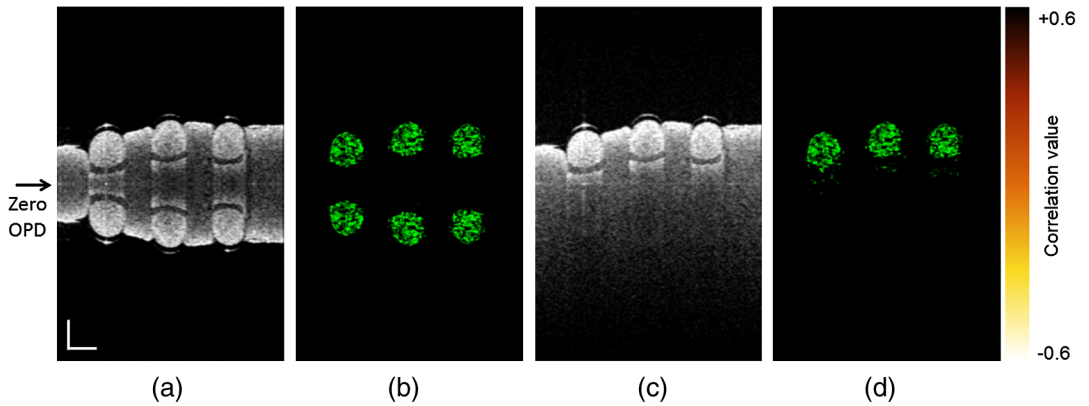

Fig. 3 Cross-sectional view of structural and flow image using conventional and full-range cm-OCT methods. (a) Structural OCT image with conventional cm-OCT (Video 1, MOV, 2.62 MB) [URL: http://dx.doi.org/10.1117/1.JBO.19.2.021103.1]. (b) Flow image with conventional cm-OCT (Video 2, MOV, 3.13 MB) [URL: http://dx.doi.org/10.1117/1.JBO.19.2.021103.2]. (c) Structural OCT image with full-range cm-OCT (Video 3, MOV, 4.64 MB) [URL: http://dx.doi.org/10.1117/1.JBO.19.2.021103.3]. (d) Flow image with full-range cm-OCT (Video 4, MOV, 2.24 MB) [URL: http://dx.doi.org/10.1117/1.JBO.19.2.021103.4]. In the color bar, the higher correlation is shown as darker color, while lower correlation is shown as brighter color. Scale bar is 500 μm.

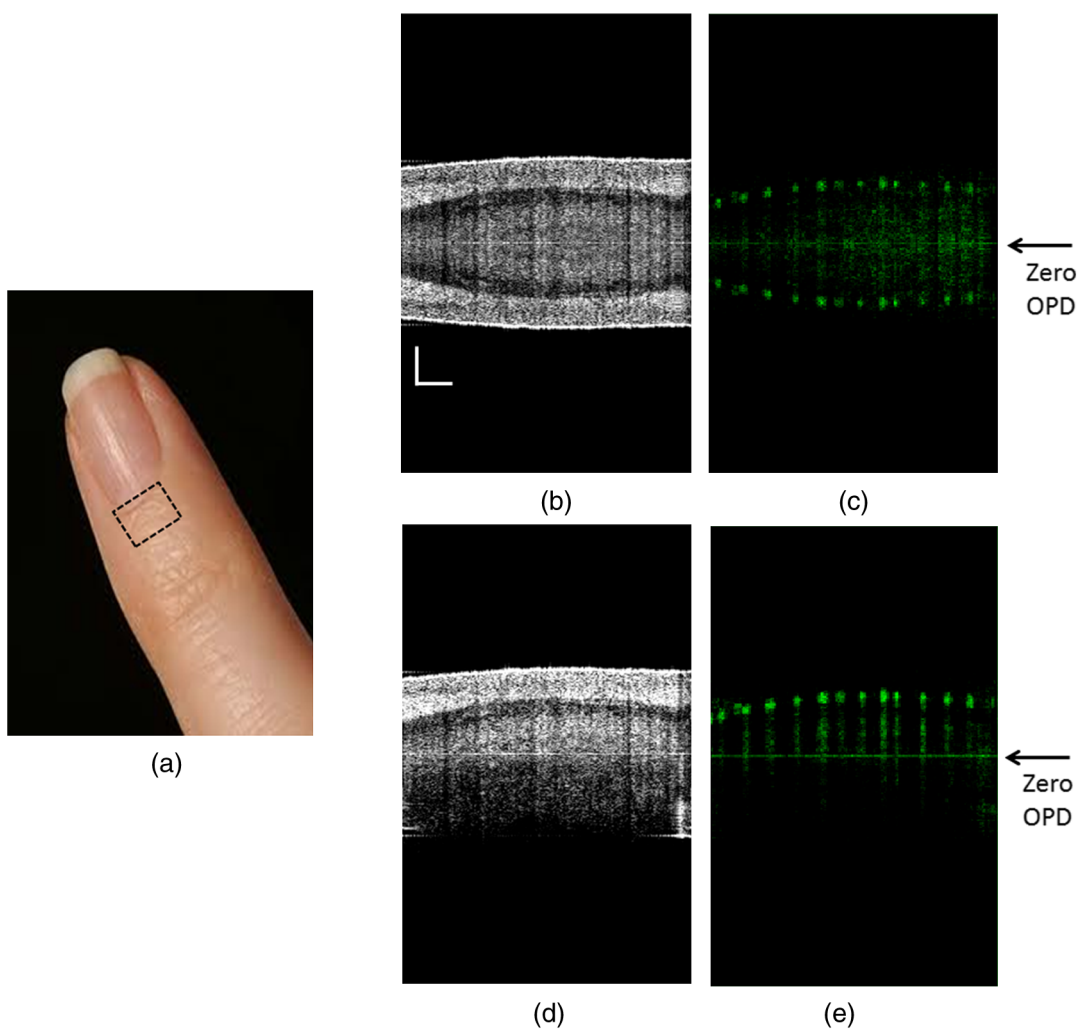

Fig. 4 Cross-sectional view of structural and microcirculation image at the base of the dorsal nail-fold area using the conventional and full-range cm-OCT methods. (a) Photograph of the region of scan at the nail-fold area with a dimension of 4 mm × 3 mm. (b) Structural OCT image with conventional spectral-domain processing. (c) Microcirculation image based on conventional cm-OCT processing. (d) Structural OCT image with full-range cm-OCT processing method (Video 5, MOV, 4.38 MB) [URL: http://dx.doi.org/10.1117/1.JBO.19.2.021103.5]. (e) Complex-conjugate-free microcirculation image with full-range cm-OCT processing method (Video 6, MOV, 1.38 MB) [URL: http://dx.doi.org/10.1117/1.JBO.19.2.021103.6]. Scale bar is 500 μm.

with a kernel size of 5×5. Figure 4(b) and 4(c) shows the cross-sectional view of structural image and the corresponding correlation-mapping flow image with conventional spectral-domain processing method. As described above, the true image is hindered by the mirror image due to the complex conjugate artifact. Figure 4(d) (Video 5) and 4(e) (Video 6) shows the corresponding fly-through of the cross-sectional structural and cm-OCT flow image using the full-range complex conjugate removal algorithm. These results clearly show the capability of full-range cm-OCT to provide complex-conjugate-free full-range cm-OCT flow image with additional benefits of doubling the measurement range for both structural and microcirculation imaging. It also enables the accessibility of high-sensitivity area near the zero-OPD, which is quite useful for various *in vivo* experiments.

Figure 5(a) (Video 7) shows the volumetric visualization rendered by merging the full-range microstructural 3-D image and the corresponding 3-D image of microcirculation with a size of $4\ \text{mm}(x) \times 3\ \text{mm}(y) \times 6\ \text{mm}(z)$ acquired with the full-range cm-OCT method. Figure 5(b) (Video 8) reveals the microcirculation map through the volume cutaway of the structural OCT image. The reconstructed cm-OCT map clearly illustrates the normal nail-fold capillary pattern. Typically, the capillary loops physiologically have a hairpin shape and are arranged in parallel longitudinal rows in the proximal nail-fold area.[34] However, the lateral resolution of our system was not good enough to clearly resolve the loops of the capillaries. By using high-numerical aperture objective lens, it could be possible to resolve the hairpin loops of the capillaries. Figure 5(c) (Video 9) shows the volumetric view of the capillary bed at the proximal nail-fold area. Figure 5(d) shows the maximum intensity projection through the entire volume of the reconstructed cm-OCT flow map.

4 Summary

In this article, we described and presented a high-speed full-range complex-conjugate-free SD cm-OCT system. By applying a beam offset method to introduce a modulation frequency and implementing a modified repeated scanning protocol, we optimized the cm-OCT reconstruction algorithm to obtain complex-conjugate-free microcirculation maps at an A-scan rate of ~91 kHz. The high-speed full-range complex-conjugate-free

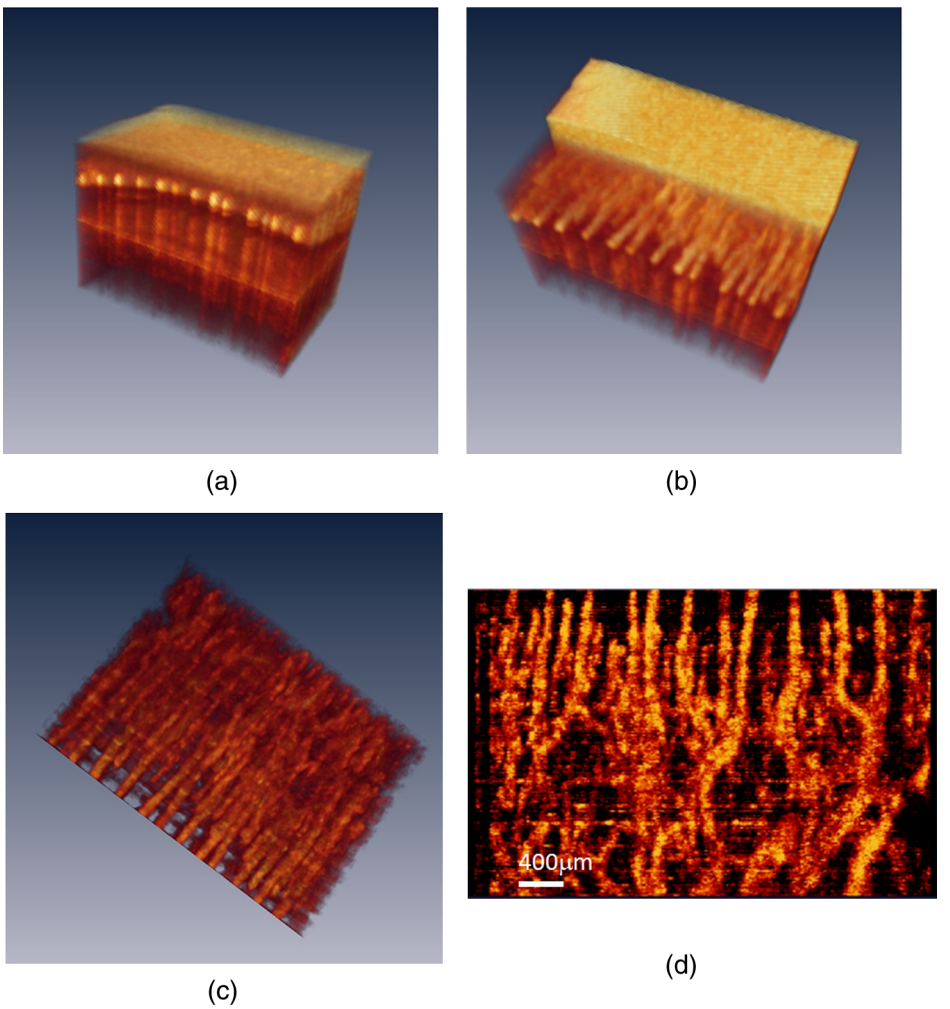

Fig. 5 Volumetric view of cm-OCT microcirculation map of the dorsal distal skin of little finger with a volume of area of 4 mm × 3 mm × 6 mm. (a) Volumetric image showing the merged volumetric full-range structural image and cm-OCT microcirculation image (Video 7, MOV, 2.01 MB) [URL: http://dx.doi.org/10.1117/1.JBO.19.2.021103.7]. (b) A longitudinally cutaway view of the 3-D volumetric full-range cm-OCT microcirculation image (Video 8, MOV, 2.02 MB) [URL: http://dx.doi.org/10.1117/1.JBO.19.2.021103.8]. (c) Volumetric full-range flow image of nail-fold capillary microcirculation (Video 9, MOV, 3.73 MB) [URL: http://dx.doi.org/10.1117/1.JBO.19.2.021103.9]. (d) Volumetric maximum intensity projection view of full-range microcirculation of the nail-fold capillary flow.

cm-OCT system was then applied to *in vivo* experiments. With these experiments, we demonstrated the superior performance of full-range cm-OCT system with modified repeated scanning protocol to provide high-speed microcirculation mapping with better contrast for wide-field imaging applications. Compared to conventional cm-OCT, full-range complex-conjugate-free cm-OCT is able to provide double measurement range and higher system sensitivity. Although we demonstrated the full-range complex imaging cm-OCT at ~91 kHz A-scan rate, the system reported here has no limitations on the imaging speed and can directly be applied to any existing high-speed Fourier-domain OCT setup to achieve volumetric *in vivo* microcirculation imaging with extended imaging depth range and high sensitivity.

Acknowledgments

This work was supported by the National Biophotonics Imaging Platform Ireland funded under the Higher Education Authority PRTLI Cycle 4, cofunded by the Irish Government and the European Union–Investing in your future. The authors also acknowledge the generous help from Dr. Joey Enfield and Mr. Roshan Dsouza, National University of Ireland, Galway.

References

1. A. F. Fercher et al., "Optical coherence tomography—Principles and applications," *Rep. Prog. Phys.* **66**(2), 239–303 (2003).
2. H. M. Subhash and R. K. Wang, "Optical coherence tomography: technical aspects," Chapter 5 in *Biomedical Optical Imaging Technologies Design and Applications*, R. Liang, Ed., pp. 163–212, Springer-Verlag, Berlin, Heidelberg (2013).
3. M. Choma et al., "Sensitivity advantage of swept source, and Fourier domain optical coherence tomography," *Opt. Express* **11**(18), 2183–2189 (2003).
4. J. F. de Boer et al., "Improved signal-to-noise ratio in spectral-domain compared with time-domain optical coherence tomography," *Opt. Lett.* **28**(21), 2067–2069 (2003).
5. R. Leitgeb, C. Hitzenberger, and A. Fercher, "Performance of Fourier domain vs. time domain optical coherence tomography," *Opt. Express* **11**(8), 889–894 (2003).
6. H. M. Subhash, "Biophotonics modalities for high resolution imaging of microcirculatory tissue beds using endogenous contrast: a review on present scenario, and prospects," *Int. J. Opt.* **2011**, 20 (2011).
7. Z. Chen et al., "Noninvasive imaging of in vivo blood flow velocity using optical Doppler tomography," *Opt. Lett.* **22**(14), 1119–1121 (1997).
8. R. Leitgeb et al., "Real-time assessment of retinal blood flow with ultrafast acquisition by color Doppler Fourier domain optical coherence tomography," *Opt. Express* **11**(23), 3116–3121 (2003).
9. B. J. Vakoc et al., "Three dimensional microscopy of the tumor microenvironment in vivo using optical frequency domain imaging," *Nat. Med.* **15**(10), 1219–1223 (2009).
10. B. J. Vakoc, G. J. Tearney, and B. E. Bouma, "Statistical properties of phase-decorrelation in phase-resolved Doppler optical coherence tomography," *IEEE Trans. Med. Imaging* **28**(6), 814–821 (2009).
11. J. Fingler et al., "Mobility and transverse flow visualization using phase variance contrast with spectral domain optical coherence tomography," *Opt. Express* **15**(20), 12636–12653 (2007).
12. A. Mariampillai et al., "Optimized speckle variance OCT imaging of microvasculature," *Opt. Lett.* **35**, 1257–1259 (2010).
13. A. Mariampillai et al., "Speckle variance detection of microvasculature using swept-source optical coherence tomography," *Opt. Lett.* **33**(13), 1530–1532 (2008).
14. E. Jonathan, J. Enfield, and M. J. Leahy, "Correlation mapping method for generating microcirculation morphology from optical coherence tomography (OCT) intensity images," *J. Biophotonics* **4**(9), 583–587 (2011).
15. J. Enfield, E. Jonathan, and M. Leahy, "In vivo imaging of the microcirculation of the volar forearm using correlation mapping optical coherence tomography (cmOCT)," *Biomed. Opt. Express* **2**(5), 1184–1193 (2011).
16. Y. Jia et al., "Split-spectrum amplitude-decorrelation angiography with optical coherence tomography," *Opt. Express* **20**(4), 4710–4725 (2012).
17. C. Blatter et al., "In situ structural and microangiographic assessment of human skin lesions with high-speed OCT," *Biomed. Opt. Express* **3**(10), 2636–2646 (2012).
18. R. K. Wang et al., "Three dimensional optical angiography," *Opt. Express* **15**(7), 4083–4097 (2007).
19. R. K. Wang and H. M. Subhash, "Optical microangiography: high-resolution 3-D imaging of blood flow," *Opt. Photonics News* **20**(11), 40–46 (2009).
20. H. M. Subhash et al., "Volumetric in vivo imaging of microvascular perfusion within the intact cochlea in mice using ultra-high sensitive optical microangiography," *IEEE Trans. Med. Imaging*, **30**(2), 224–230 (2011).
21. V. J. Srinivasan et al., "Rapid volumetric angiography of cortical microvasculature with optical coherence tomography," *Opt. Lett.* **35**(1), 43–45 (2010).
22. Y. K. Tao, A. M. Davis, and J. A. Izatt, "Single-pass volumetric bidirectional blood flow imaging spectral domain optical coherence tomography using a modified Hilbert transform," *Opt. Express* **16**(16), 12350–12361 (2008).
23. R. K. Wang and L. An, "Doppler optical micro-angiography for volumetric imaging of vascular perfusion in vivo," *Opt. Express* **17**(11), 8926–8940 (2009).
24. B. White et al., "In vivo dynamic human retinal blood flow imaging using ultra-high-speed spectral domain optical coherence tomography," *Opt. Express* **11**(25), 3490–3497 (2003).
25. Y. Yasuno et al., "In vivo high-contrast imaging of deep posterior eye by 1- um swept source optical coherence tomography, and scattering optical coherence angiography," *Opt. Express* **15**(10), 6121–6139 (2007).
26. Y. Wang et al., "Retinal blood flow detection in diabetic patients by Doppler Fourier domain optical coherence tomography," *Opt. Express* **17**(5), 4061–4073 (2009).
27. L. Yu and Z. Chen, "Doppler variance imaging for three-dimensional retina, and choroid angiography," *J. Biomed. Opt.* **15**(1), 016029 (2010).
28. A. G. Podoleanu, G. M. Dobre, and D. A. Jackson, "En-face coherence imaging using galvanometer scanner modulation," *Opt. Lett.* **23**(3), 147–149 (1998).
29. B. Baumann et al., "Full range complex spectral domain optical coherence tomography without additional phase shifters," *Opt. Express* **15**(20), 13375–13387 (2007).
30. H. M. Subhash, L. An, and R. K. Wang, "Ultra-high speed full range complex spectral domain optical coherence tomography for volumetric imaging at 140,000 A scans per second," *Proc. SPIE* **7554**, 75540K (2010).
31. L. An, H. M. Subhash, and R. K. Wang, "Full range complex spectral domain optical coherence tomography for volumetric imaging at 47 000 A-scans per second," *J. Opt.* **12**(8), 084003 (2010).
32. L. An and R. K. Wang, "Use of a scanner to modulate spatial interferograms for in vivo full-range Fourier-domain optical coherence tomography," *Opt. Lett.* **32**(23), 3423–3425 (2007).
33. H. M. Subhash and M. Leahy, "High-speed high-sensitivity spectral-domain correlation mapping optical coherence tomography based modified scanning protocol," *Proc. SPIE* **8571**, 85712I (2013).
34. Y. Kabasakal et al., "Quantitative nail-fold capillaroscopy findings in a population with connective tissue disease, and in normal healthy controls," *Ann. Rheum. Dis.* **55**(8), 507–512 (1996).